https://doi.org/10.5194/egusphere-2026-3022
Preprint. Discussion started: 14 July 2026

A Maxwell-Based Dual-Morphology Wet Snow Microstructure Model for Liquid Water Amount Retrieval in Greenland's Percolation Zone Using SMAP L-Band Radiometry

Hui Jiang[1], Firoz Borah[1], Leung Tsang[1], Zhenming Huang[1], Alamgir Hossan[2], Andreas Colliander[3]

[1]Radiation Laboratory, Department of Electrical Engineering and Computer Science, University of Michigan, Ann Arbor, MI 48109, USA
[2]Jet Propulsion Laboratory, California Institute of Technology, La Cañada Flintridge, CA 91011, USA
[3]Finnish Meteorological Institute, Helsinki, 00560, Finland

Correspondence to: Hui Jiang (huijia@umich.edu)

Abstract. Liquid water amount (LWA) in seasonal snow controls meltwater retention, refreezing, and runoff. The retrieval of LWA from L-band brightness temperature (TB) observations remains highly sensitive to the effective permittivity of wet snow. Classical wet snow microstructure studies indicate that low liquid water content (LWC) wet snow contains both interfacial/contact-scale liquid and thicker localized pore-space water, whereas existing mixing formulas assume a single liquid water morphology. In this paper, we introduce a Maxwell-based dual-morphology wet-snow model that partitions liquid water between thin-coated interfacial water and localized thicker Tri-continuous (Tri-C) water through a morphology parameter (α) defined as the fraction of the total liquid water assigned to the thin-coated component. A permittivity database generated from computer-generated microstructures and numerical Maxwell solutions is used to train a neural-network emulator for retrieval. For a representative case with LWC = 2% and snow density 400 kg/m^3, varying α from 0 to 1 increases the imaginary part of the effective permittivity by a factor of 37, demonstrating first-order morphology-control on L-band dielectric loss. We combine this model with a two-layer radiative transfer framework and a temporally constrained inversion of the vertically and horizontally polarized SMAP TB at six Greenland percolation-zone AWS sites (CP1, DY2, KAN_U, NSE, SDL, and SDM) to retrieve α, LWC, wet layer thickness, and LWA. The retrieval reproduces the observed morning-pass seasonal evolution and suggests relatively larger thin-coated contributions at melt onset, Tri-C dominance during peak melt, and an incomplete late-season return toward thin-coated dominance, likely due to incompletely refrozen earlier meltwater. These results show that explicit liquid-water morphology can substantially improve L-band retrieval of wet snow compared with traditional mixing models.

1 Introduction

Liquid water amount (LWA) in seasonal snow and firn is a key variable governing meltwater retention, refreezing, and runoff, and therefore plays an important role in snow hydrology, ice sheet surface mass balance, and broader climate impacts

https://doi.org/10.5194/egusphere-2026-3022
Preprint. Discussion started: 14 July 2026

during the melt season (Greene et al., 2024; Hossan et al., 2025a; Houtz et al., 2021; Khan et al., 2015, 2022; Mouginot et al., 2019; Otosaka et al., 2023; The IMBIE Team, 2020). Passive microwave radiometry provides an attractive means to monitor meltwater over large areas, but conventional higher frequency observations (>6GHz) penetrate only shallowly into wet snow and saturate at small amounts; thus, primarily indicating surface or near-surface melt occurrence rather than the vertically integrated liquid water stored within the snow/firn column (Colliander et al., 2022, 2023; Hossan et al., 2025a). In contrast, L-band radiometry at 1.4 GHz, as provided by missions such as NASA Soil Moisture Active Passive (SMAP) (Entekhabi et al., 2026), offers substantially greater penetration and has emerged as a promising tool for retrieving subsurface liquid water and total LWA (Hossan et al., 2025a, b; Houtz et al., 2019, 2021). However, converting L-band brightness temperatures (TB) into LWA requires an accurate calculation of the effective permittivity of wet snow, because both the real and especially the imaginary parts of the permittivity control absorption, emission, and penetration depth. Different wet snow permittivity mixing formulas can lead to substantially different retrieved LWA values (Hossan et al., 2025a; Picard et al., 2022).

Classical approaches for estimating the effective permittivity of wet snow have largely relied on dielectric mixing formulas that trade physical realism for analytical simplicity. Many analytical formulations are derived for idealized inclusion geometries, typically spherical or ellipsoidal particles embedded in a host medium, with the geometry entering through depolarization factors or related parameters (Jones and Friedman, 2000; Sihvola, 1999). Such shapes do not accurately represent the complex microstructures of wet snow. In real dry snow, the ice phase is commonly organized as irregularly shaped grain clusters rather than as isolated ideal particles; wet snow further consists of a three-phase mixture of air, ice grains, and liquid water. In real wet snow microstructures, liquid water may reside in grain-contact fillets and veins, evolve through pendular to funicular regimes, and interact with an irregular and dynamically changing pore space (Denoth, 1982). A second class of models is empirical, in which the effective permittivity is fitted directly to laboratory or field measurements over specific ranges of frequency, density, temperature, and wetness (Hallikainen et al., 1986; Tiuri et al., 1984), without a physical basis. In addition, their transferability beyond the range of measurements on which they were based remains inherently uncertain. This uncertainty is not merely conceptual: (Hossan et al., 2025a) systematically compared ten widely used wet snow dielectric models and showed that they produce substantial spreads in both the real and imaginary parts of the effective permittivity, which in turn lead to markedly different LWA from the same observations.

Bi-continuous (Bi-C) media provide a physically motivated alternative to classical particle-based descriptions of dry snow microstructure (Ding et al., 2010). Earlier studies showed that computer-generated Bi-C realizations bear good resemblance to images of real dry snow and can reproduce key geometric descriptors of snow, such as correlation structure and specific surface area (SSA), while naturally representing irregular, clustered ice-air interfaces rather than idealized isolated particles (Chang et al., 2014; Ding et al., 2010; Xu et al., 2012; Zhu et al., 2023). Building on this idea, tri-continuous (Tri-C) media was proposed to represent wet snow (Huang et al., 2024). The Tri-C extends the framework from two phases to three, thereby enabling the representation of wet snow as a coupled ice-water-air system, with liquid water introduced as a third continuous phase surrounding the melting ice (Huang et al., 2024). A key advantage of the Bi-C/Tri-C approach is that the

https://doi.org/10.5194/egusphere-2026-3022
Preprint. Discussion started: 14 July 2026

effective permittivity is not prescribed by an analytical mixing rule but is instead obtained from first principles by numerically solving the Maxwell equations on computer-generated microstructures. In Huang et al. (2024), each realization is illuminated electromagnetically, its scattering and absorption responses are computed, and the effective permittivity is then retrieved by matching these responses to those of an equivalent homogeneous sphere through Mie theory. In this sense, the Bi-C/Tri-C framework provides a Maxwell-equation-based route from physically plausible snow morphology to macroscopic effective permittivity.

Although the Tri-C framework represents a major advance beyond classical mixing formulas, its baseline wet snow realizations still place liquid water mainly in relatively compact, localized regions. For the Greenland percolation zone considered here, however, the radiometrically relevant regime for L-band retrieval is typically a low-LWC regime, with liquid water volume fractions on the order of about 0 %–6 % (Hossan et al., 2025a). In this low wetness regime, the classical wet snow literature suggests that the liquid phase should not be viewed as a single fully connected water body. Instead, the classical picture developed by Colbeck and Denoth (Colbeck and Parssinen, 1978; Denoth, 1982) indicates that wet snow at low saturation is generally in the pendular state, in which liquid water is concentrated around grain contacts and along narrow intergranular pathways. Denoth (1982) described this low-saturation liquid geometry in terms of menisci, fillets, and veins, and further noted that, at very low saturation, the liquid geometry is controlled by water menisci surrounding the contact points of ice grains. In parallel, Colbeck and Parssinen (1978) explicitly discussed pressure melting at inter-particle contacts and the presence of a thin liquid film separating neighboring ice particles. Taken together, these studies suggest that one physically relevant part of low LWC wet snow liquid water is an interfacial or contact-scale component, which in the present work is represented effectively by the thin-coated water component. At the same time, Denoth (1982) also showed that, as liquid saturation increases even within the low LWC pendular-to-transitional regime, the veins become progressively filled with water and the liquid distribution becomes increasingly controlled by these thicker liquid structures. This second part of the classical picture suggests the presence of localized thicker pore-space water bodies, which in the present work are represented by the Tri-C water component. In this sense, the present dual-morphology description follows the classical physical picture of low LWC wet snow: one component represents the interfacial/contact-scale liquid (thin-coated water), and the other represents the thicker localized liquid structures (Tri-C water).

The coexistence of these two physically motivated liquid-water components naturally leads to a dual-morphology wet snow model. Accordingly, in the present work, the total liquid water is partitioned between thin-coated water and Tri-C water, with the former serving as an effective representation of the thin interfacial/contact-scale liquid implied by the classical literature, and the latter serving as an effective representation of the thicker fillet-, vein-, bridge-, and pore-space liquid structures that become increasingly important as wetness grows. This morphology partitioning has major electromagnetic consequences: As will be shown later in this paper, even for a fixed LWC of 2% and a snow density of 400kg/m^3, the imaginary part of the effective permittivity changes by about a factor of 37 as the thin-coated water fraction varies from 0 to 1. This strong sensitivity indicates that liquid-water morphology exerts first-order control on the L-band radiometric response in the low LWC regime relevant to Greenland percolation-zone retrievals. We therefore introduce the thin-coated

https://doi.org/10.5194/egusphere-2026-3022
Preprint. Discussion started: 14 July 2026

water fraction as an explicit morphology parameter and use the vertically and horizontally polarized SMAP TB (TB_v and TB_h, respectively) observations to infer not only the amount of liquid water, but also the partitions between thin-coated and Tri-C water that evolve through the melt season at six Greenland AWS sites (Brodzik et al., 2021; Fausto et al., 2021).

2 Dual-Morphology Wet Snow Model

To represent the dielectric behavior of low-LWC wet snow more realistically (within 6% for Greenland percolation zone Hossan et al. (2025a)), we introduce a dual-morphology wet snow model that recasts the classical low-wetness picture of wet snow into a Maxwell-compatible effective geometry. The purpose of this section is to define the interfacial/contact-scale configurations and thicker localized pore-space structures of the liquid-water components, introduce the morphology parameter α that partitions the total liquid water between them, and then describe how this morphology partitioning affects the effective permittivity of wet snow.

2.1 Physical meaning of Tri-C water and thin-coated water

The dual-morphology model is intended for low LWC wet snow in the pendular or pendular-to-transitional regime. In this regime, classical studies indicate that liquid water distribution is controlled strongly by both liquid saturation and snow structure. In particular, (Denoth, 1982) showed that, at very low saturation, the liquid geometry is controlled by water menisci surrounding the contact points of ice grains, whereas with increasing saturation, fillets and veins develop and the veins become progressively filled with water. This classical picture motivates the two effective liquid-water components used here.

The first component is referred to as thin-coated water. In the present work, this component serves as an effective representation of the interfacial and contact-scale liquid implied by the classical low-wetness picture, i.e. the surface-bound liquid associated with the earliest stage of melting. The term thin-coated is therefore used as a compact model label for this interfacial liquid component.

The second component is referred to here as Tri-Continuous (Tri-C) water. In the present work, this component serves as an effective representation of the relatively thicker and more localized liquid-water phase occupying pore-space regions within the snow microstructure. Physically, it is intended to describe thicker liquid structures such as localized water pockets, water bridges between nearby ice structures, and vein-like pore-space connections, which become increasingly important as wetness grows. The term Tri-C is retained because the present model builds on the previously developed Bi-C/Tri-C framework, but it is used here as a practical label for the localized thicker liquid phase rather than as a claim that the liquid always forms a single idealized tri-continuous geometry.

Taken together, these two components provide a compact effective description of low LWC wet snow: thin-coated water represents the interfacial/contact-scale liquid emphasized in the classical literature, whereas Tri-C water represents the thicker localized pore-space liquid structures. The detailed numerical realization of these two components is described later in Section. 2.4.

https://doi.org/10.5194/egusphere-2026-3022
Preprint. Discussion started: 14 July 2026

2.2 Definition of the dual-morphology model and the parameter α

Having introduced the two effective liquid-water components, we partition the total liquid water content (LWC) between them through a morphology parameter α, where $0 \leq \alpha \leq 1$. Let V_{snow} denotes the total volume of the wet snow and V_{water} denotes the total liquid water volume. In this study, liquid water content, LWC us defined as the liquid water volume fraction of snow:

$$\mathrm{LWC} = \frac{V_{water}}{V_{snow}} \tag{1}$$

The morphology parameter α is defined as the fraction of the total liquid water volume assigned to the thin-coated component:

$$\alpha = \frac{V_{thin-coated\ water}}{V_{water}} \tag{2}$$

Therefore, the liquid water volume fractions of the two components relative to the total wet snow volume are written as

$$f_{v,film} = \alpha LWC,\ \ f_{v,Tri-C} = (1-\alpha)LWC \tag{3}$$

Under this definition, $\alpha = 0$ corresponds to the limiting case in which all liquid water is assigned to the localized thicker component (all Tri-C water), and no thin-coated water is present. In contrast, $\alpha = 1$ corresponds to the opposite limiting case in which all liquid water is assigned to the thin-coated component. Intermediate values $0 \leq \alpha \leq 1$ represent mixed morphologies in which interfacial/contact-scale liquid and thicker localized liquid coexist.

The liquid water amount, LWA, is obtained by integrating LWC over the wet snow layer thickness d_{wet}.

$$\mathrm{LWA} = \ \mathrm{LWC}{\cdot}d_{wet}[m] \cdot 1000\ \ [mm] \tag{4}$$

Thus, LWC describes the volumetric concentration of liquid water within the wet layer, d_{wet} describes the thickness of that layer, and LWA represents the equivalent vertical water depth in millimeters.

Importantly, α should be interpreted as an effective morphology parameter rather than as a directly observed geometric fraction. Its role is to preserve the total LWC while isolating how the partition of liquid water between these two physically motivated components affects the effective permittivity. This definition is particularly useful in the present low-LWC setting, because later sections show that redistributing the same total amount of liquid water between these two end members can produce a large change in dielectric loss, and that the inferred α can evolve through the melt season.

2.3 Illustration of the Tri-C, thin-coated, and dual models

Figure 1 schematically illustrates the three water-morphology cases considered in the present low LWC wet snow model. In the pure Tri-C case ($\alpha = 0$), all liquid water is assigned to the localized thicker component, so the water phase appears only as discrete thicker pore-space regions within the snow microstructure. In the pure thin-coated case ($\alpha = 1$), all liquid water is assigned to the interfacial component, so the water phase appears as thin coatings attached to the surfaces of ice. In the mixed dual-morphology case ($0 \leq \alpha \leq 1$), both components coexist, with the relative partition between them controlled by α.

https://doi.org/10.5194/egusphere-2026-3022
Preprint. Discussion started: 14 July 2026

2.4 Computer Generation of the dual morphology

The dual-morphology model is implemented by extending the previously developed Bi-C/Tri-C random medium framework, in which snow microstructures are generated from computer-generated random fields and material phases are assigned through thresholding (Ding et al., 2010; Huang et al., 2024). In particular, the baseline Tri-C component follows the computer-generation procedure described by (Huang et al., 2024), where a random medium function S(r) is first generated from a superposition of random cosine waves, as given in their Eq. (5), and the ice, water, and air phases are then assigned using the two threshold rule in their Eq. (8), with the thresholds determined from the prescribed ice and water volume fractions through their Eqs. (9) and (10). In the present work, we retain this general framework, but replace the single liquid-water morphology with a partitioned liquid phase consisting of two components: a localized thicker Tri-C component and a thin-coated interfacial component.

This construction should be viewed as an effective numerical realization of the classical low-LWC wet snow picture, rather than as a literal geometrical reproduction of any single historical model. Classical studies indicate that, in low LWC snow, liquid water may occur both as interfacial/contact-scale liquid and as thicker liquid structures associated with fillets, veins, and localized pore-space water. The present dual-morphology implementation is designed to capture these two physically distinct tendencies within a Maxwell-compatible numerical geometry.

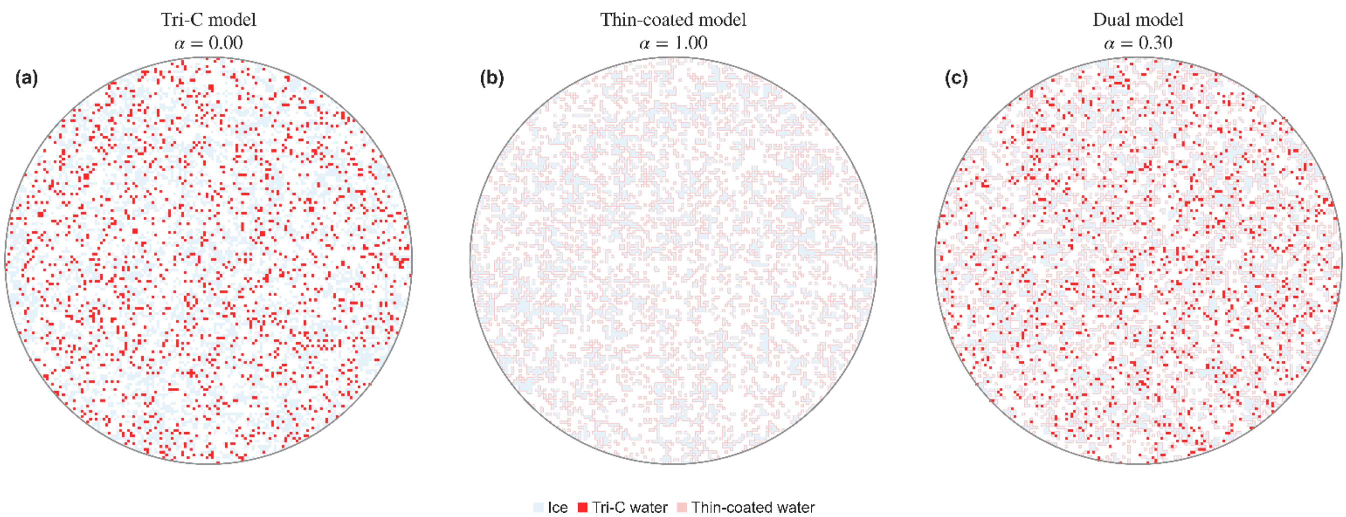

Figure 1: Schematic representation of the three water morphologies considered in the proposed dual wet snow model: (a) pure Tri-C morphology ($\alpha = 0$), (b) pure thin-coated morphology ($\alpha = 1$), and (c) mixed dual morphology ($\alpha = 0.3$). Red is used for Tri-C water and light pink for thin-coated water to visually distinguish the two morphological components and improve readability; these colors are schematic only and do not imply physical optical colors. The thin-coated water is visually enlarged for clarity.

For a prescribed snow density ρ_s, the ice volume fraction is set as

$$f_{v,i} = \rho_s / \rho_i \tag{5}$$

Where ρ_i is the ice density. For a prescribed liquid water content (LWC) and morphology parameter α, the total liquid water volume fraction is partitioned according to Eq. (3). In the present implementation, the thin-coated component is realized

https://doi.org/10.5194/egusphere-2026-3022
Preprint. Discussion started: 14 July 2026

numerically as an interfacial water film attached to randomly selected ice-air interfacial faces, whereas the remaining water is assigned to the Tri-C component. The Tri-C component is discretized on cubic water cells with edge length 0.5mm, i.e. each cell acts as a numerical voxel of the localized thicker liquid phase. Accordingly, in the present model, Tri-C water has a minimum resolved thickness of about 0.5mm, while thicker Tri-C regions are naturally represented when multiple adjacent 0.5mm cells are connected. In this sense, the Tri-C component represents the relatively thicker pore-space liquid structures, in contrast to the ultrathin interfacial liquid represented by the thin-coated component.

The thin-coated component is represented by a $10\mu m$ interfacial water layer. This choice is motivated by two considerations. First, the thin-coated component is intended to represent the interfacial/contact-scale liquid emphasized in the classical low-LWC pendular picture of wet snow. Second, measurements of frictional meltwater on snow reported meltwater layer thicknesses of about 4-20 μm under conditions where only a very small amount of meltwater is generated and the water remains confined to a thin interfacial layer rather than developing into thicker localized liquid bodies(Siddiqui et al., 2024). Although this frictional melt setting differs from natural wet snow metamorphism, it provides a useful experimental thickness scale for the thin-coated end member. We therefore adopt 10 μm as a physically reasonable representative thickness for the thin-coated component. Because the morphology is discretized numerically, the realized phase fractions are checked a posteriori for each realization to verify consistency with the prescribed snow density, LWC, and morphology parameter α.

2.5 Calculations of the Effective Permittivity from Numerical Solutions of 3D Maxwell Solutions

A key feature of the present approach is that the effective permittivity is calculated from numerical solutions of 3D Maxwell's equations, rather than prescribed by a classical dielectric mixing formula. This distinction is important because Maxwell's equations govern precisely all the electromagnetic phenomenon in microwave radiometry, whereas classical mixing formulas rely on simplified constitutive assumptions(Sihvola, 1999). Many analytical mixing formulas are derived for highly idealized inclusion geometries, typically spherical or ellipsoidal particles embedded in a host medium, with the morphology represented through depolarization factors or related parameters(Sihvola, 1999). Such assumptions are difficult to reconcile with wet snow, which is a complex three phase mixture of air, ice and liquid water. In real wet snow microstructures, liquid water may occupy irregular pore-space regions, bridges, veins, and thin interfacial coatings.

A second class of models is empirical, in which the effective permittivity is fitted directly to laboratory or field measurements over restricted ranges of frequency, density, temperature, and LWC (Hallikainen et al., 1986; Tiuri et al., 1984; Ulaby and Long, 2014). The difficulty is that, as will be shown later in this paper, the effective permittivity can change strongly even when the LWC and snow density are fixed, simply because the liquid water morphology changes. In particular, variation in the thin-coated water fraction α can produce a very large change in the imaginary part of the effective permittivity. We will also show later that α evolves during the melt season. Thus, field measurements collected at different stages of melt season may correspond to substantially different underlying morphologies. If morphology is not explicitly

https://doi.org/10.5194/egusphere-2026-3022
Preprint. Discussion started: 14 July 2026

represented, these different states may be mixed together in an empirical parameterization, thereby limiting its physical interpretability and predictive transferability.

In contrast, the present method evaluates the electromagnetic response directly on computer-generated dual-morphology snow microstructures by solving 3D Maxwell's equations numerically, thereby retaining the geometric complexity of the medium. In the present work, Maxwell's equations are solved numerically using Ansys HFSS(Ansys Hfss, n.d.), which is based on the finite element method (FEM) (Jin, 2014). HFSS is adopted here because FEM is particularly well suited to highly inhomogeneous media such as the present dual-morphology wet snow microstructure, which contains irregular ice-air-water interfaces together with a strong disparity of length scales between the $10\mu m$ thin-coated water and the Tri-C component, whose minimum resolved thickness is 0.5mm. Its adaptive unstructured tetrahedral meshing allows local refinement near complex interfaces and thin layers while retaining geometric flexibility throughout the heterogeneous volume. The resulting scattering and absorption responses of each realization are then used to retrieve the effective permittivity by matching them to those of an equivalent homogeneous sphere through Mie theory. This extraction framework follows the previously developed Bi-C/Tri-C permittivity methodology of (Huang et al., 2024) and is therefore not repeated here in full detail. The new element in the present work is not the Maxwell-based extraction procedure itself, but the extension of the wet-snow morphology from a single Tri-C water configuration to a dual-morphology model consisting of localized thicker Tri-C water and thin-coated interfacial water.

2.6 Sensitivity of the Effective Permittivity to Liquid Water Morphology

To quantify the electromagnetic consequence of the morphology partitioning, we consider a representative case in which the LWC is fixed at 2%, and the snow density is fixed at $\rho_s = 400 kg/m^3$. Figure 2 shows the corresponding variation of the effective permittivity as α increases from 0 to 1. Here, $\alpha = 0$ corresponds to the limiting case of the previous single-Tri-C wet snow morphology, whereas $\alpha = 1$ corresponds to the opposite limit in which all liquid water is assigned to the thin-coated component.

The real part of the effective permittivity increases moderately as α increases. In contrast, the imaginary part exhibits a much stronger sensitivity to morphology. In this representative case, the real part increases from 1.975 at $\alpha = 0$ to 2.763 at $\alpha = 1$, whereas the imaginary part increases from 0.0034 to 0.126, i.e., by about a factor of 37. This result shows that, even when the LWC and snow density are fixed, redistributing the same total amount of liquid water from localized thicker Tri-C regions into thin interfacial coatings can dramatically enhance dielectric loss.

To understand this behavior physically, it is useful to recall that wet snow consists of three constituents: air, ice, and liquid water. Among these three components, air and ice are nearly lossless at L-band, whereas liquid water has a much larger imaginary permittivity and is therefore the dominant absorber. The local absorption inside the water phase is governed by the dissipated power density,

https://doi.org/10.5194/egusphere-2026-3022
Preprint. Discussion started: 14 July 2026

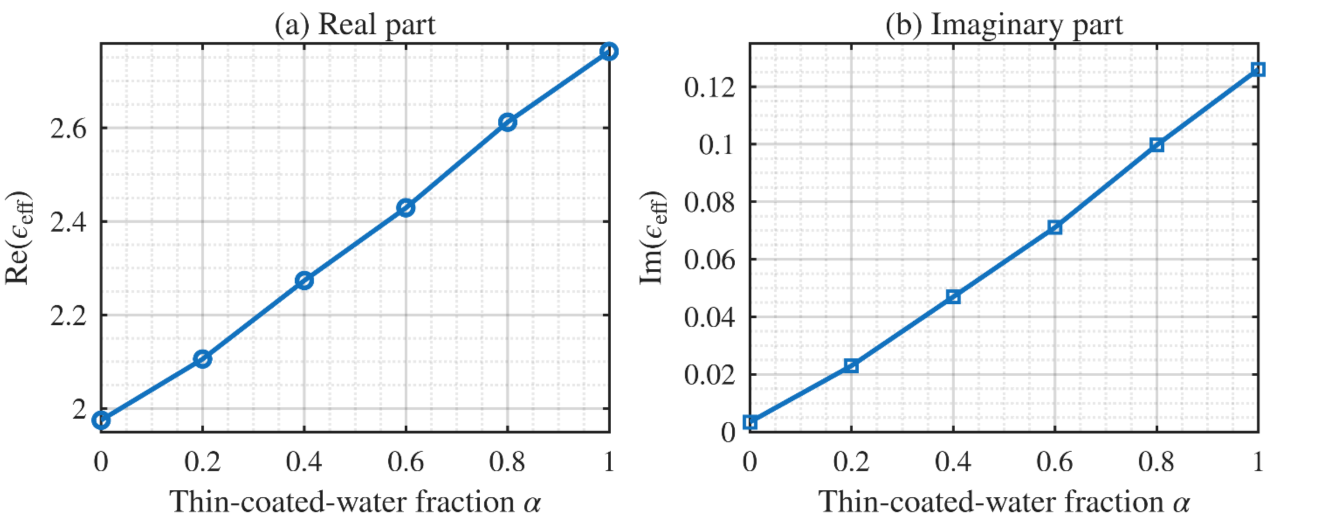

Figure 2: Variation of the effective permittivity of the dual-morphology wet snow model with α for a representative case with LWC fixed at 2% and $\rho_s = 400kg/m^3$: (a) real part and (b) imaginary part. The real part increases from 1.975 at $\alpha = 0$ to 2.763 at $\alpha = 1$, whereas the imaginary part shows a much stronger sensitivity, increasing from 0.0034 at $\alpha = 0$ to 0.126 at $\alpha = 1$, i.e., by about a factor of 37.

$$P_{abs} = \frac{1}{2}\omega\varepsilon_0\varepsilon''_{water}|E_{water}|^2 \tag{6}$$

So for a given liquid water permittivity ε_{water} (imaginary part ε''_{water}), morphology affects dielectric loss primarily through the internal electric field distribution within the water phase E_{water} and through how much of the water volume overlaps with strong field regions.

A useful physical intuition follows from the electromagnetic boundary conditions. The tangential component of the electric field is continuous across the interface, whereas the normal component of the electric displacement satisfies $D_n = \varepsilon E_n$. Therefore,

$$E_{t,water} = E_{t,out}, \;\; \varepsilon_{water}E_{n,water} = \varepsilon_{out}E_{n,out} \tag{7}$$

Because the permittivity of liquid water at L-band is much larger than that of air or ice (denoted by out), the normal electric field inside water is strongly suppressed, whereas the tangential field can remain comparatively large. Thus, the electric field that effectively penetrates into the water phase is dominated primarily by its tangential component near water-air or water-ice interfaces.

A useful analogy can also be drawn from classical effective medium theory. In generalized Maxwell-Garnett mixing formulas, the geometry of the liquid water inclusion is not irrelevant: it enters through the depolarization factors of spheroidal or ellipsoidal inclusions. As discussed by (Sihvola, 1999), extreme inclusion shapes such as disk can produce a much larger imaginary part of the effective permittivity than spherical inclusions for the same inclusion volume fraction. This classical result already indicates that the electromagnetic effect of liquid water is controlled not only by the total water volume, but also by how that water is geometrically distributed and how the local electric field is established inside the lossy phase. A disk-like or film-like water morphology has a much larger interfacial-area-to-volume ratio than a compact spherical

https://doi.org/10.5194/egusphere-2026-3022
Preprint. Discussion started: 14 July 2026

inclusion. Therefore, for the same amount of liquid water, a much larger fraction of the water volume is located close to water-air or water-ice interfaces, where the tangential electric field can couple efficiently into the water phase. The same physical idea applies to the present dual-morphology model. When liquid water is assigned to the thin-coated component, the prescribed water volume is spread into ultrathin interfacial layers attached to many ice-air interfacial faces. This produces a very large interfacial area per unit water volume. In contrast, when the same amount of liquid water is assigned to the Tri-C component, the water is concentrated into more compact localized pore-space bodies. Such compact Tri-C water has a much smaller interfacial-area-to-volume ratio, so a larger fraction of the water volume is located away from the interface-associated strong-field regions and experiences a weaker local internal field. Thus, the stronger dielectric loss of the thin-coated case should be interpreted as a morphology induced local field and interfacial exposure effect. This interpretation is consistent with, but more general than, the classical Maxwell Garnett argument: in both cases, changing the water morphology while keeping the total water volume fixed changes the volume averaged electric field inside the lossy water phase and therefore changes the imaginary part of the effective permittivity.

Snow Density (kg/m^3)	LWC	α	$\lvert E\rvert_{water}^{mean}$ (V/m)
400	2%	0	0.0756
400	2%	1	0.4101

Table 1: Mean internal electric field amplitude within the water phase for the representative case with LWC=2% and snow density $400kg/m^3$. For both cases, the incident electric field amplitude in Ansys HFSS is set to 1 V/m.

The numerical results are consistent with this interpretation. Table 1 shows that, for this representative example, the mean internal electric field amplitude within the water phase is much larger in the pure thin-coated case ($\alpha = 1$) than in the pure Tri-C case ($\alpha = 0$): it increases from 0.0756 to 0.4101 V/m, even though the incident electric field amplitude in HFSS is set to 1 V/m in both simulations. Thus, redistributing the same total amount of liquid water from localized thicker Tri-C regions into thin interfacial coatings places much more of the lossy water in a geometry that supports a strong internal electric field and therefore efficient absorption. This stronger field concentration in the thin-coated limit helps explain the much larger imaginary part of the effective permittivity when α approaches 1.

More generally, these results show that liquid water morphology exerts first-order control on the effective permittivity of low LWC wet snow. In particular, they demonstrate that the effective permittivity cannot be represented reliably as a function of snow density and LWC alone. Most classical wet snow dielectric mixing formulas are parameterized only by bulk variables such as snow density and LWC(Hallikainen et al., 1986; Hossan et al., 2025a; Jones and Friedman, 2000; Sihvola, 1999; Tiuri et al., 1984), and therefore do not explicitly account for the presence of thin-coated interfacial water or for the partition of liquid water between thin-coated and localized thicker components. By contrast, the present dual-morphology model introduces the morphology parameter α, so that the effective permittivity is described not only by snow density and LWC, but also by the liquid water morphology itself. In this sense, the $\alpha = 0$ limit recovers the previous single Tri-C morphology(Huang et al., 2024), whereas intermediate and large α values represent additional thin-coated water states that can produce much larger dielectric loss. This morphology dependence is therefore one of the main motivations for

https://doi.org/10.5194/egusphere-2026-3022
Preprint. Discussion started: 14 July 2026

introducing the dual-morphology wet snow model, and later sections will show that the inferred thin-coated water fraction indeed evolves through the melt season.

2.7 Comparison with conventional wet snow mixing formulas

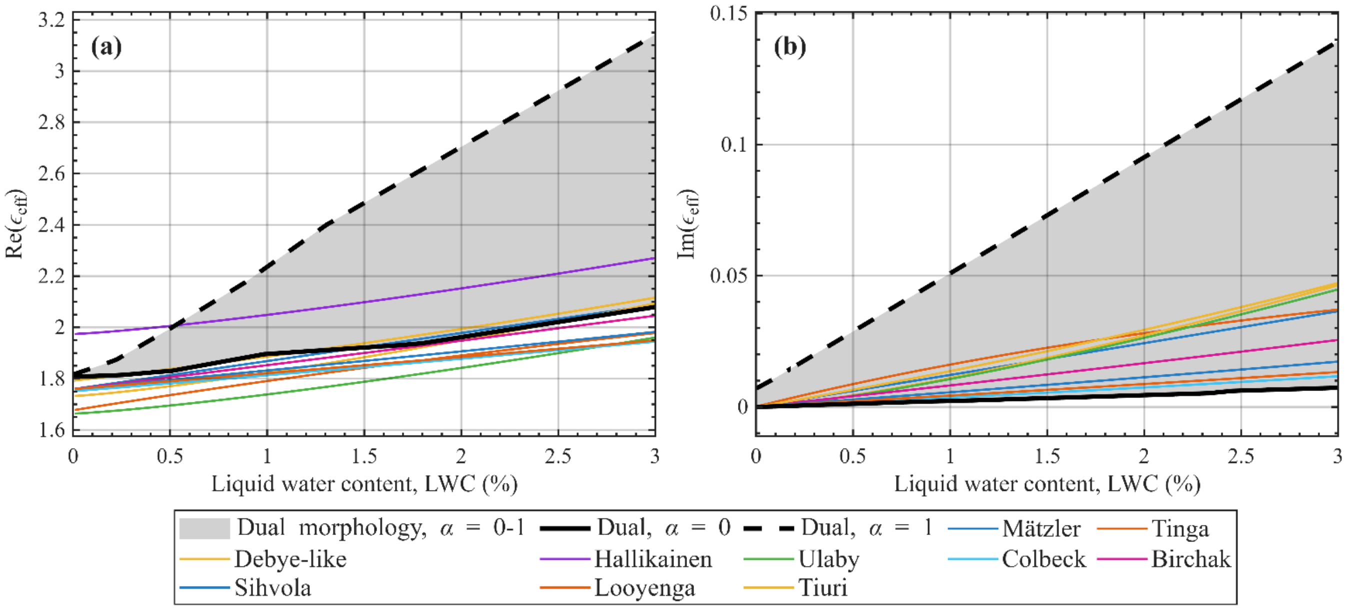

Figure 3: Comparison of wet snow effective permittivity predicted by conventional wet snow mixing formulas used in (Hossan et al., 2025a) and the dual-morphology wet snow model for LWC from 0 to 3% at snow density of 400 kg/m^3: (a) real part and (b) imaginary part.

The sensitivity analysis in Section 2.6 shows that, for a fixed LWC and snow density, the effective permittivity can vary strongly depending on how the liquid water is distributed between localized thicker Tri-C water and thin-coated water. To place this morphology-induced variability in the context of commonly used wet-snow dielectric models, Figure 3 compares the proposed Maxwell-based dual-morphology model with a set of conventional wet-snow mixing formulas used in (Hossan et al., 2025a). The comparison is made for 1.4GHz, snow density of 400 kg/m^3, and LWC from 0% to 3%. For the dual-morphology model, the grey shaded region denotes the range of effective permittivity obtained by varying the thin-coated water fraction α from 0 to 1 at each LWC. The black solid curve corresponds to the pure Tri-C limit ($\alpha = 0$), whereas the black dashed curve corresponds to the pure thin-coated limit ($\alpha = 1$).

As shown in Figure 3, the conventional mixing formulas generally produce monotonic increases in ε_{eff} as LWC increases. For a fixed snow density and frequency, each of these formulas essentially maps a given LWC to a single effective permittivity value. Therefore, although different formulas give different absolute values because of their different empirical or theoretical assumptions, they do not explicitly represent the effect of liquid water morphology. In other words, they cannot distinguish whether the same amount of liquid water is distributed as localized thicker pore-space water, thin interfacial water, or a mixture of the two.

https://doi.org/10.5194/egusphere-2026-3022
Preprint. Discussion started: 14 July 2026

By contrast, the proposed dual-morphology model predicts a range of possible effective permittivities at the same LWC, depending on the value of α. This behavior is especially evident in the imaginary part, where the grey shaded region is much wider than the spread among most conventional formulas. The comparison indicates that liquid-water morphology introduces an additional degree of freedom that is not captured by traditional LWC-based mixing formulas. Thus, the effective permittivity of low-LWC wet snow is not only controlled by the total amount of liquid water, but also by how that liquid water is geometrically distributed within the snow microstructure.

3 Retrieval framework for wet snow morphology and layer properties from SMAP L-band radiometry

In this section, we describe the retrieval framework used to infer the wet snow state variables from SMAP L-band radiometry. The retrieved variables are the thin-coated water fraction α, LWC, and the effective wet layer thickness d_{wet}, from which SMAP pass scale liquid water amount (LWA) is also derived. Because a single SMAP pass provides only two radiometric observables TB_v and TB_h, whereas the wet snow state is described by three unknowns, the retrieval is formulated as a seasonally constrained inverse problem rather than a pass-by-pass fit. The subsections below describe the neural network permittivity emulator, the forward radiative model, the seasonal inversion strategy, and the post-retrieval dry screening.

3.1 Neural Network Permittivity Emulator

A direct optimization of the wet-snow state variables requires a fast mapping from the morphology and bulk wetness parameters to the corresponding effective permittivity. To achieve this, we use a neural network permittivity emulator trained on the numerical Maxwell permittivity database introduced in Section 2(Hornik et al., 1989; Rumelhart et al., 1986). The inputs of the emulator are the thin-coated-water fraction α, LWC, and the snow density ρ_s, and the output is the corresponding complex effective permittivity ε_{eff}.

For each candidate state proposed by the retrieval, the emulator provides the corresponding effective permittivity almost instantaneously. The optimizer then uses this predicted ε_{eff} in the forward radiative model to evaluate the candidate state against the observed SMAP brightness temperatures.

3.2 Two Layer Radiative Transfer Forward Model

To connect the unknown wet snow state variables to the observed SMAP brightness temperatures, we use a two layer radiative transfer forward model. The upper layer is a pass-dependent wet layer described by the state variables to be inferred, namely α, LWC, and d_{wet}. The lower layer represents the deeper dry firn background. This two-layer model is an approximation, adopted because an explicit multilayer model would introduce too many unknown profile parameters.

For each study site and polarization ($p = v, h$), we use the mean dry-season SMAP brightness temperature, TB_p^{dry} obtained by averaging the January-April observations at that site, as the radiometric contribution from the bottom dry firn.

https://doi.org/10.5194/egusphere-2026-3022
Preprint. Discussion started: 14 July 2026

With this approximation, the two layer RT forward model is written as:

$$TB_p = (1 - r_p)(T_s(1 - e^{-\tau \sec(\theta)}) + TB_p^{dry} e^{-\tau \sec(\theta)}) \tag{8}$$

Where $p = v, h$ denotes the polarization, r_p is the power reflectivity of the upper wet layer air interface at polarization p which depends on ε_{eff} of the wet layer, T_s is the wet layer temperature. In the present study, T_s is taken from the in-situ measurement at the six study sites(Fausto et al., 2021). If such measurement are unavailable, $T_s = 273.15K$ provides a practical wet season approximation, since the near surface wet layer is typically close to melting point during sustained melt conditions. TB_p^{dry} is the mean dry-season SMAP brightness temperature for polarization p, and θ is the SMAP incident angle. τ represents the optical depth of the wet layer and depends on both the ε_{eff} of the wet layer and the d_{wet}. Thus, the factor $e^{-\tau \sec(\theta)}$ represents the attenuation of the lower layer dry firn contribution as the signal propagates through the absorptive wet layer. When the wet layer is weakly absorbing or thin, the observed brightness temperature remains close to the dry-season background; when the wet layer becomes more absorptive or thicker, the lower layer contribution is increasingly suppressed and the signal becomes dominated by the upper wet layer. The detailed formulas used to compute the reflectivities, attenuation coefficient, and their dependence on ε_{eff} are provided in section 3.2 of the Supplementary Information.

3.3 Temporally Constrained Time-Series Retrieval

A single SMAP overpass provides only two radiometric observables, TB_v and TB_h, whereas the wet snow state is described here by three unknowns: the thin-coated water fraction α, the liquid-water content (LWC), and the effective wet layer thickness d_{wet}. In the present implementation, the snow density is not retrieved but fixed at $400 kg/m^3$, following the representative near surface density level reported for the study region in (Hossan et al., 2025a). The inverse problem is therefore still underdetermined at pass scale, because many different combinations of (α,LWC,d_{wet}) can produce nearly the same pair (TB_v, TB_h). For this reason, the retrieval is not formulated as a pass-by-pass fit, but as a seasonally constrained inversion.

The retrieval is designed to select one physically coherent seasonal path from many locally admissible candidates. For each SMAP pass, we first construct a candidate library by sampling α over five intervals, spanning compact Tri-C dominated states to more thin-coated, film-like states, and by sampling LWC within the allowed wetness range (<6%). For each (α, LWC) candidate, the neural network permittivity emulator provides the corresponding effective permittivity. The wet layer thickness d_{wet} is then solved analytically from the two layer radiative transfer model, rather than sampled as a third grid dimension. This reduces computational cost and avoids an unnecessarily broad unconstrained search over depth.

Each candidate is evaluated with a local objective function that contains one primary radiometric term and several weak regularization terms. The primary term is the two polarization mismatch between observed and simulated SMAP TB_v and TB_h. The regularization terms do not provide independent observations of liquid water; instead, they guide the selection among candidates that fit the radiometry similarly well. These terms include a weak seasonal LWA shape guide derived from the dry-referenced SMAP TB anomaly, wet state admissibility, soft prior and boundary penalties, and a late season penalty that suppresses unrealistic residual LWA during refreezing or dry like conditions.

Because the SMAP TB shape information is used as a weak regularization term, it should not be interpreted as an independent validation dataset. In the next section, the scaled SMAP TB shape function is shown only as a timing indicator of the observed L-band wetting signal. Independent physical context is provided by comparison with SAMIMI and GEMB(Gardner et al., 2023; Samimi et al., 2020, 2021) and by consistency with the observed polarization and seasonal behavior.

The preliminary wet season retrieval is obtained by dynamic programming. Instead of selecting the best local candidate independently at each SMAP pass, the algorithm searches for the lowest cost seasonal path through all candidate libraries. The transition cost penalizes physically implausible jumps in α, LWC, d_{wet}, and LWA, and includes a directional term that encourages LWA to increase when the SMAP wetness signal increases and to decrease when it decreases.

This formulation should be interpreted as a regularized time-series inversion. The physical forward model and the two polarization TB fit provide the direct radiometric constraint, while the additional terms stabilize an underdetermined inverse problem and suppress implausible solutions. The full mathematical definition of the candidate library, local cost terms, dynamic programming transition cost, dry screening diagnostics, and all weighting and normalization parameters is provided in the Supplementary Information. A representative sensitivity and ablation test is also provided there to evaluate the influence of the weak SMAP TB shape guide, the post-retrieval dry screen, and the main regularization and temporal-coupling weights on the retrieved seasonal evolution.

3.4 SMAP Brightness Temperature Signatures and Post-Retrieval Dry Screening

The retrieval is guided not only by the absolute values of the SMAP brightness temperatures, but also by the physical meaning of their seasonal evolution. Figure 4 shows the 2023 SMAP vertically polarized and horizontally polarized brightness temperatures at the six study sites, namely CP1, DY2, KAN_U, NSE, SDL, and SDM. These are the same six Greenland percolation-zone AWS sites and the same melt year considered in (Hossan et al., 2025a). For consistency with that study, we use the enhanced-resolution twice-daily rSIR SMAP brightness temperature product on the EASE-2 3.125 km grid, colocated with the six PROMICE and GC-Net sites.

The need for post-retrieval dry screening arises directly from the simplified forward model adopted in Section 3.2. In that model, the deeper dry firn contribution is represented by the January-April mean dry season SMAP brightness temperature for each site and polarization. This approximation is practical and suitable for large scale retrieval, but it also implies that any pass whose observed brightness temperature differs from the January-April reference can, in principle, be interpreted by the forward model as requiring a nonzero wet layer at the top. This interpretation is reasonable during active melt, but it is not always correct outside the melt season. In particular, after the main wet season, the snow/firn column may already have returned to a dry-like state while still exhibiting a radiometric baseline that differs slightly from the January-April mean (especially during November), because the melt season can modify the snow microstructure through meltwater percolation,

https://doi.org/10.5194/egusphere-2026-3022
Preprint. Discussion started: 14 July 2026

refreezing, and the formation of internal ice layers(Charalampidis et al., 2016; Rennermalm et al., 2022). In such cases, a retrieval based only on the forward-model fit may incorrectly assign a small amount of liquid water to the upper layer, even though the pass is physically dry.

The dry screening is designed to remove this class of artificial weak wet solutions. It uses time-series signatures that are difficult to capture with an absolute TB threshold alone. Dry like periods tend to have a large and stable V-H polarization separation, whereas active melt produces a strong increase in TB and a collapse of the polarization contrast. Morning-evening differences provide an additional diagnostic: daytime wetting often raises evening TB and reduces the polarization contrast relative to the morning pass, while dry conditions have weaker and more stable diurnal differences. After the melt season, recovery of a large and stable polarization separation is interpreted as dry-like behavior even when the absolute TB baseline remains seasonally shifted.

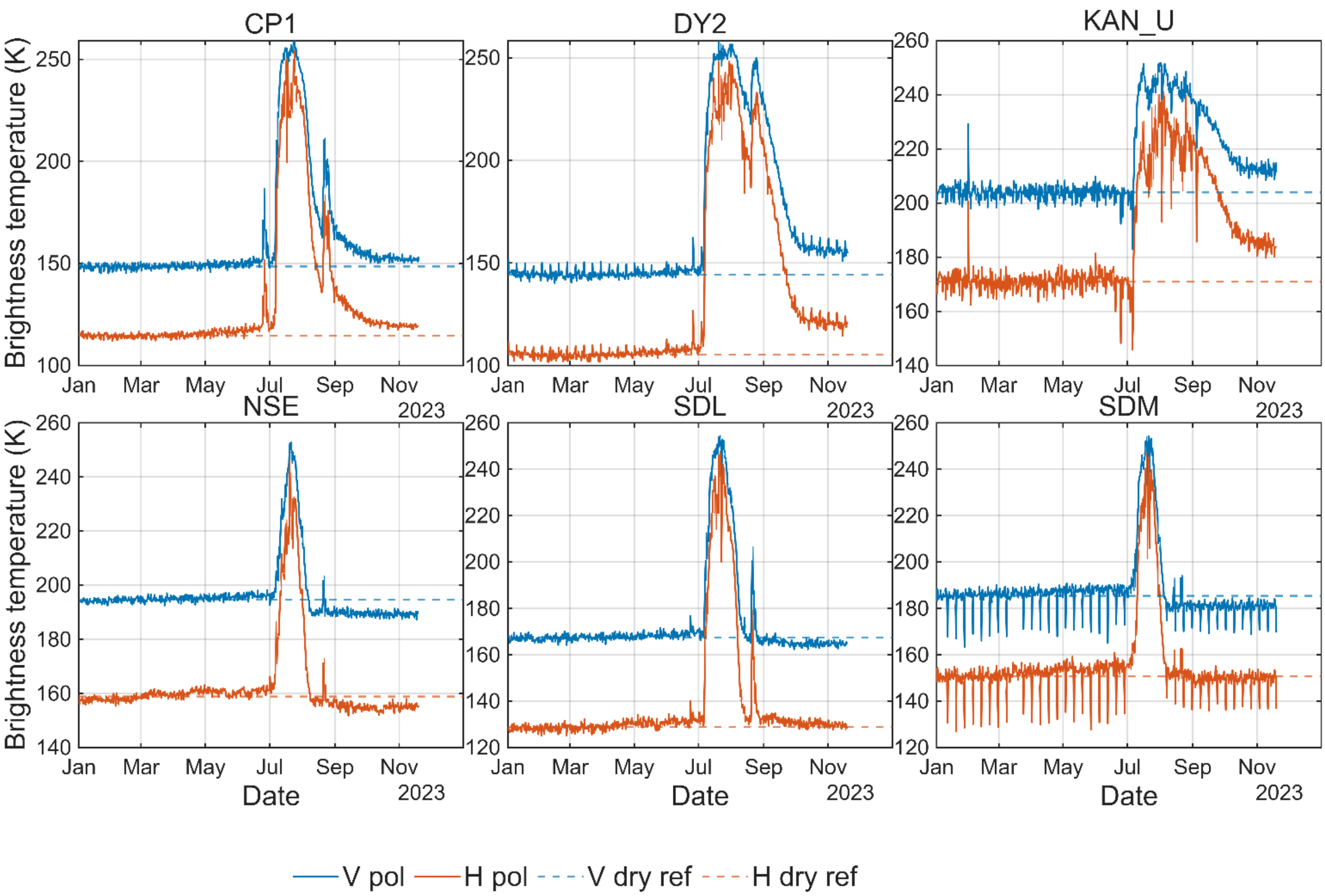

Figure 4: SMAP vertically polarized (TB_v) and horizontally polarized (TB_h) brightness temperature during 2023 at the six study sites used in this work. Dashed lines denote the January-April mean dry-season brightness temperatures for the two polarizations.

These time-series signatures are central to the retrieval strategy. In the retrieval, every SMAP pass is first treated as a potentially wet pass, and the three wet snow state variables (α,LWC,d_{wet}) are preliminarily retrieved under the forward

https://doi.org/10.5194/egusphere-2026-3022
Preprint. Discussion started: 14 July 2026

model. This wet-first step is intentional, because it avoids prematurely rejecting weak but physically meaningful melt signals near melt onset or during late-season refreezing. However, this preliminary wet-first retrieval is not always sufficient to identify dry conditions after the main melt season. In particular, during the post-melt dry period, especially in November, the snow/firn column may have returned to a physically dry state while the observed brightness temperatures remain shifted from the January-April dry season reference. Because the two layer forward model uses this January-April mean as the deeper dry firn background, such a shifted dry baseline can be incorrectly fitted by introducing a small nonzero wet layer at the top. The post retrieval dry screen is therefore applied mainly to remove these artificial weak-wet solutions in the post-melt dry season. SMAP passes are classified as dry when the seasonal TB evolution, recovery and stability of the polarization separation, and morning-evening diagnostics indicate dry-like behavior. For those passes, the final reported wet variables are set to zero, i.e., α,LWC,d_{wet} and LWA =0.

The detailed diagnostic definitions and thresholds are provided in the Supplementary Information. The Supplementary Information also includes a no-dry-screen sensitivity case, which illustrates what happens if the preliminary wet first retrieval is used directly without the post retrieval dry screen. In that case, weak residual wet states can persist after the main melt season, especially during the post melt period when the observed brightness temperature baseline remains shifted from the January-April dry reference. This behavior supports the use of the dry screening step to remove artificial weak wet solutions rather than interpret them as physical liquid water. In the brightness temperature comparison shown later in Fig. 4, some late season dry like passes, especially those in November with a shifted radiometric baseline, are still displayed using the preliminary wet first simulated TB values before dry screening; these points are not used to interpret the final retrieved LWA or morphology after dry screening.

4 Results and Physical Interpretation

In this section, we evaluate the proposed retrieval model using the SMAP observations and independent model based references. We first assess radiometric agreement by comparing the brightness temperatures simulated by our model with the observed SMAP brightness temperatures. We then examine whether the wet snow states retrieved by our model provide a physically plausible picture of the seasonal evolution of meltwater storage and liquid water morphology. In particular, we evaluate whether our model can reproduce the observed L-band signal while remaining consistent with the expected timing, intensity, and persistence of meltwater during the melt season. We also assess whether the variations in wet layer thickness d_{wet} and thin-coated water fraction α inferred by our model reflect physically meaningful changes in the distribution of liquid water, rather than merely providing a numerical fit to the brightness temperatures.

4.1 Comparison between Simulated and Observed SMAP Morning Pass Brightness Temperatures

Figure 5 compares the simulated and observed SMAP brightness temperatures at the six study sites. Because the retrieval uses only the morning SMAP passes, the comparison is restricted to the morning pass (10:30) TB_v and TB_h. At all six sites, both TB_v and TB_h are well matched by the predicted brightness temperatures. The retrieval reproduces the main seasonal

https://doi.org/10.5194/egusphere-2026-3022
Preprint. Discussion started: 14 July 2026

evolution of the observed L-band signal, indicating that the inferred wet-snow states capture the dominant radiometric behavior at both polarizations.

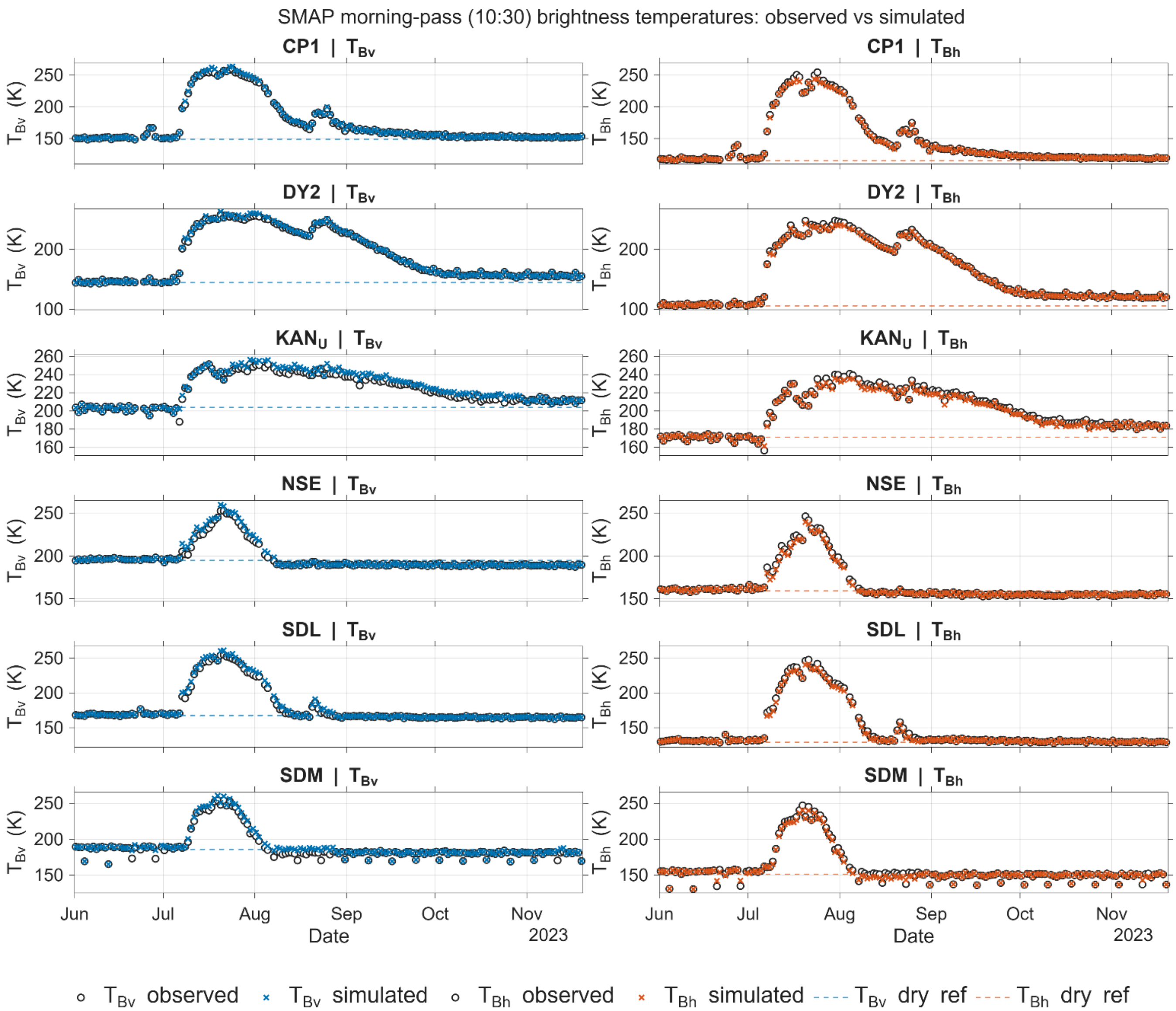

Figure 5: Comparison between observed and simulated SMAP morning-pass (10:30) brightness temperatures at the six study sites

4.2 Retrieved Liquid Water Amount (LWA) Compared with SAMIMI and GEMB

Figure 6 compares the retrieved LWA in mm with two independent surface energy and mass balance (SEMB) references, namely the locally calibrated SAMIMI model and the GEMB model(Gardner et al., 2023; Samimi et al., 2020, 2021). Here, SAMIMI can be viewed as a locally calibrated site-scale reference that focuses on how surface meltwater penetrates, is retained, and refreezes within the near-surface firn column, whereas GEMB is a physically based glacier/firn energy and

https://doi.org/10.5194/egusphere-2026-3022
Preprint. Discussion started: 14 July 2026

mass balance column model that represents surface atmosphere energy and mass exchange together with firn state evolution. Following (Hossan et al., 2025a), both models are driven by the same in-situ AWS measurements from PROMICE and GC-Net, including hourly air temperature, air pressure, upwelling and downwelling shortwave and longwave radiation, snow-surface height, and wind speed, and are initialized with subsurface profiles of temperature, density, and stratigraphy(Fausto et al., 2021). The scaled SMAP TB shape function is also shown to highlight the timing of the observed L-band wetting signal. Because a weak version of this seasonal shape information is used in the retrieval regularization, it should be interpreted only as a timing indicator, not as an independent validation of LWA.

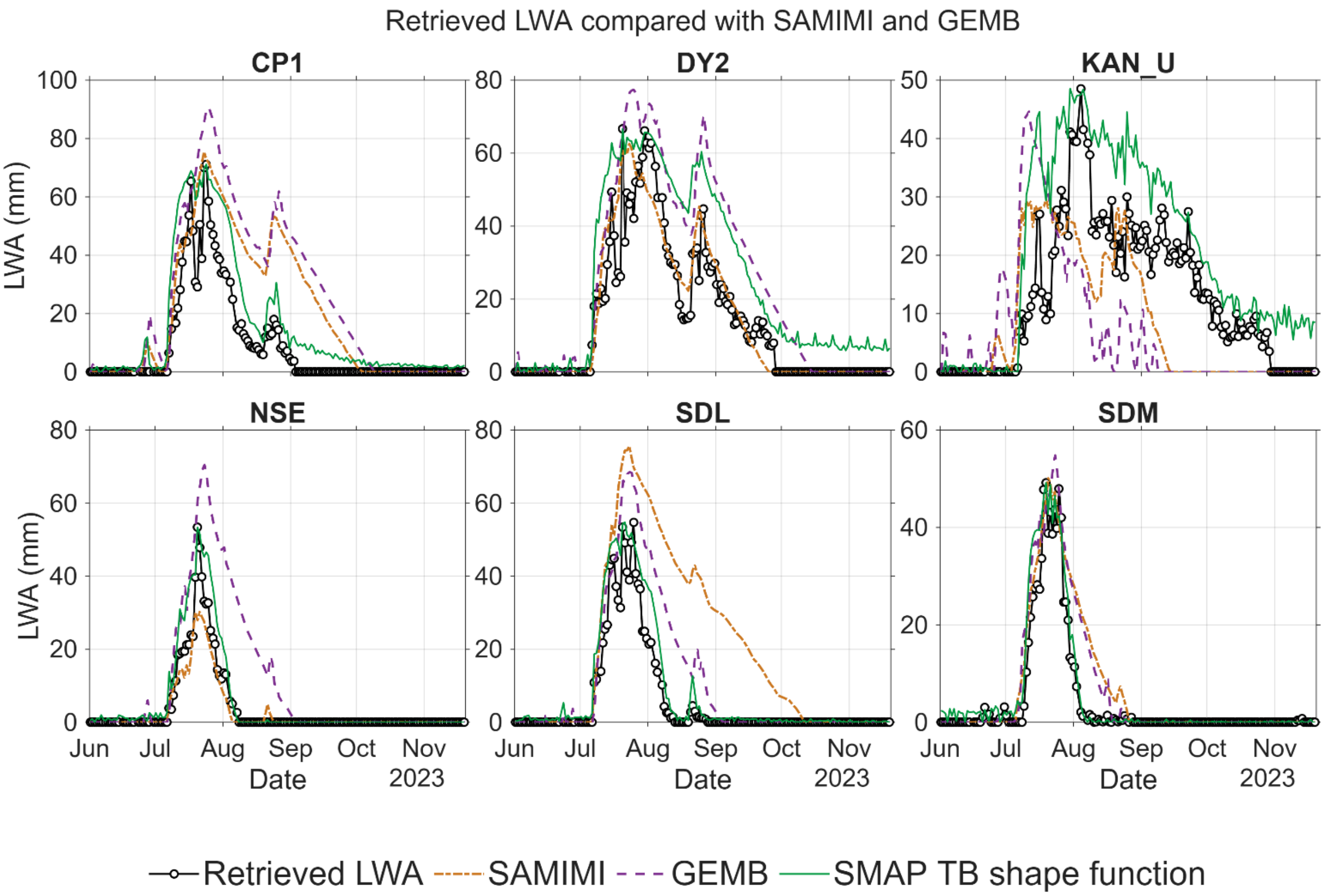

Figure 6: Comparison of the retrieved LWA in mm with the SAMIMI and GEMB surface energy and mass balance model at the six study sites during the 2023 melt season. Black circles show the retrieved LWA, the orange dash-dotted curve shows the SAMIMI results, and the purple dashed curve shows the GEMB results. The green curve shows the scaled SMAP TB shape function.

Overall, the retrieved LWA follows the general temporal structure indicated by the SMAP TB shape function at all six sites. The agreement with SAMIMI and GEMB is generally strongest for melt onset and the main melt episodes, whereas the largest differences appear in late-season persistence. In particular, KAN_U stands out as the most notable case: the SMAP

https://doi.org/10.5194/egusphere-2026-3022
Preprint. Discussion started: 14 July 2026

TB shape function indicates sustained strong melt conditions, while both SAMIMI and GEMB show much weaker melt or even little melt during part of this period. By contrast, the present retrieval continues to indicate substantial LWA there, and is therefore more consistent with the observed radiometric evolution. Across the other five sites, the two SEMB models generally show more prolonged melt than suggested by the SMAP TB shape function, whereas the retrieval tends to return to dry-like conditions more rapidly after the main melt event.

These comparisons should nevertheless be interpreted with caution. As discussed by (Hossan et al., 2025a), SAMIMI and GEMB are physically based references rather than ground truth, and the two models can produce noticeably different LWA estimates even when forced with the same in-situ AWS measurements from PROMICE and GC-Net. This difference arises because the two models use different parameterizations and model configurations for meltwater infiltration, refreezing, retention, and firn evolution. (Hossan et al., 2025a) also noted that both models tend to retain subsurface liquid water for too long during the late refreezing phase, leading to an overly prolonged melt signal. In this context, the more rapid late season decline obtained here at CP1, DY2, NSE, SDL, and SDM should not necessarily be viewed as a deficiency of the retrieval; rather, it may indicate that the retrieval is consistent with the observed SMAP L-band radiometric evolution.

4.3 Retrieved Wet-Layer Thickness

Figure 7 shows the retrieved effective wet layer thickness d_{wet} at the six study sites during the 2023 melt season. In contrast to LWA, d_{wet} is not compared here with an independent reference; instead, it is used to interpret how the retrieved liquid water is distributed vertically within the near surface snowpack. A common seasonal pattern is evident at all six sites: d_{wet} is close to zero before melt onset, then increases as the wet layer develops, reaches a site dependent maximum during the main melt period, and finally decreases back toward zero as the melt season ends. Despite site-to-site differences in duration and short term variability, this shared evolution is physically consistent with progressive wetting of the near-surface firn, followed by drainage and/or refreezing during the late melt season. At all six sites, the retrieval indicates meter scale wetting, with peak d_{wet} generally in the range of about 2-2.5m. Such values are physically plausible for the Greenland percolation zone. At DYE-2, (Samimi et al., 2020) reported that meltwater percolated to the depth of about 2m.

The site-to-site differences in d_{wet} are also physically meaningful. DY2 and KAN_U show the most prolonged meter scale wet layers, consistent with the more persistent melt behavior already seen in the SMAP brightness temperatures and in the retrieved LWA. CP1 also reaches a wet layer thickness of more than 2 m during the main melt period, but the layer thins more rapidly afterward, with a secondary late-season enhancement. SDL exhibits a similar main thickening phase, followed by a comparatively rapid collapse and a brief secondary pulse. By contrast, NSE and SDM show shorter, more pulse like wetting events, with d_{wet} increasing rapidly during the main melt episode and then returning quickly toward zero. Overall, these results indicate that the site-to-site differences in retrieved LWA reflect not only differences in total liquid water storage, but also differences in how deeply and how persistently the near-surface firn becomes wetted.

https://doi.org/10.5194/egusphere-2026-3022
Preprint. Discussion started: 14 July 2026

4.4 Seasonal Evolution of Thin-Coated and Tri-C Contributions

Figure 8 decomposes the retrieved LWA into a thin-coated component, $\alpha \cdot \mathrm{LWA}$, and a Tri-C component, $(1-\alpha) \cdot \mathrm{LWA}$, at the six study sites. The black curve denotes the total retrieved LWA, the orange shaded area represents the thin-coated contribution, and the blue shaded area represents the Tri-C contribution. Because both colored components are scaled by the total LWA, their absolute magnitudes reflect not only the morphology partition but also the total amount of liquid water present. Therefore, the quantity most directly related to morphology is the relative share of the two colored components within the total-LWA envelope: a larger orange fraction indicates a larger thin-coated water fraction α, whereas a larger blue fraction indicates stronger Tri-C dominance.

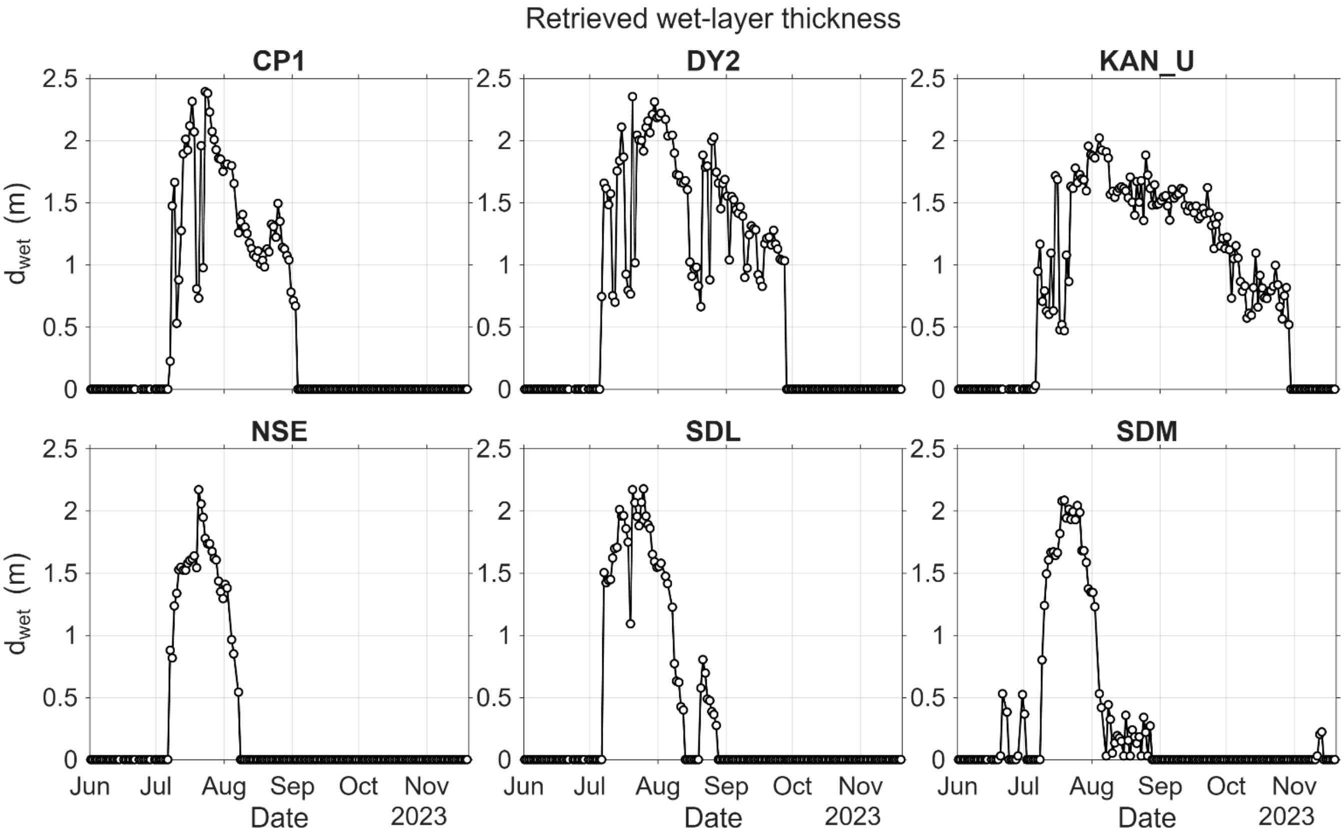

Figure 7: Retrieved effective wet-layer thickness d_{wet} at the six study sites during the 2023 melt season.

At melt onset, the total retrieved LWA is still very small, and Figure 8 shows that a relatively larger share of this limited amount is assigned to the thin-coated component. This is physically reasonable because melting begins by converting the ice surface itself into liquid water, so the earliest meltwater is expected to appear first in interfacial and contact-scale configurations, before enough liquid accumulates to form thicker and more spatially localized Tri-C water bodies. This interpretation is supported by additional wet-snow studies. (Colbeck and Parssinen, 1978) described wet snow in terms of pressure melting at inter-particle contacts and explicitly considered thin liquid films separating neighboring ice particles. (Brun, 1989)'s low liquid content wet snow experiments further showed that, in this regime, the liquid phase remains discontinuous until higher wetness is reached, while the earliest stage of wet metamorphism is marked first by a rapid change in crystal shape rather than by the immediate development of a fully continuous water phase. In the present dual-model framework, this early, small-amount, interfacial liquid is therefore most naturally represented by a relatively large α.

As melt intensifies, the partition in Figure 8 shifts systematically toward the Tri-C component, which becomes dominant during the peak melt season, even though the thin-coated amount isolated in Figure 9 may still increase at first. The physical picture is that, once meltwater production becomes substantial, only a limited amount of liquid can remain sustained in a surface- or interfacial-water-dominated state. In other words, the available ice surface and contact-scale geometry can host only a limited interfacial liquid budget, so additional meltwater cannot be accommodated simply by further increasing surface-bound water; instead, it must increasingly collect into thicker pore-scale bodies, bridges, and more spatially extended liquid pathways, represented here by the Tri-C component. This is why the retrieved thin-coated-water volumetric fraction, $\alpha \cdot$LWC, may rise into the order of 1%, but does not continue to scale with the full increase in total meltwater. The measurements in (Denoth, 1982) support the reasonableness of this magnitude: for old, coarse-grained firn, the irreducible liquid saturation is about 2–4% of pore volume, which, for the representative near-surface density used in this study, corresponds to a retained pendular-side liquid budget of order 1–2% of bulk volume. In this sense, the larger, the larger $\alpha \cdot$LWC peaks at CP1, DY2 and KAN_U, approaching ~2%, and the smaller peaks at NSE, SDL, and SDM, of order 0.8%, are both physically plausible. This interpretation is also consistent with (Colbeck and Parssinen, 1978)'s distinction between low liquid content clustered wet snow and higher liquid content wet snow with stronger liquid connectivity, and with (Brun, 1989)'s finding that the liquid phase remains discontinuous at low wetness but that increasing liquid-water content promotes the formation of longer continuous paths. In the present dual-morphology framework, melt intensification is therefore characterized not by the disappearance of thin-coated water, but by the fact that its limited surface-bound storage capacity is increasingly exceeded, so the additional meltwater is routed preferentially into the Tri-C component and the main melt period becomes progressively Tri-C dominated.

Toward the end of the melt season, the amount of newly produced meltwater becomes small again, so by analogy with melt onset one might expect the liquid-water morphology to revert to a thin-coated water dominated state. The retrieval suggests that this return is incomplete. The key reason is that, unlike melt onset, the late melt season does not begin from a previously dry state: some liquid water produced earlier in the season may remain unfrozen rather than having fully refrozen. Direct support for such late-season retained liquid comes from Greenland firn studies. (Charalampidis et al., 2016) showed that, in the lower accumulation area of southwest Greenland, the upper 2.5 m of snow and firn remained temperate during the melt season, while meltwater percolation and refreezing beneath 2.5 m depth only occurred after the melt season. (Forster et al., 2014) demonstrated that substantial subsurface liquid water can persist through winter in Greenland firn. A plausible interpretation is that this residual liquid is more likely to be associated with the Tri-C component than with the thin-coated component, because thicker and more localized liquid bodies are expected to refreeze less readily than very thin interfacial

https://doi.org/10.5194/egusphere-2026-3022
Preprint. Discussion started: 14 July 2026

water. In the present dual model framework, the late season state can therefore be viewed as a superposition of two effects: only a small amount of newly generated meltwater, which by itself would again favor thin-coated water, together with some inherited, incompletely refrozen residual liquid from earlier melt periods, which is more naturally represented by Tri-C water.

Table 2 provides a concise conceptual summary of the three characteristic stages of the retrieved water-morphology evolution during the melt season.

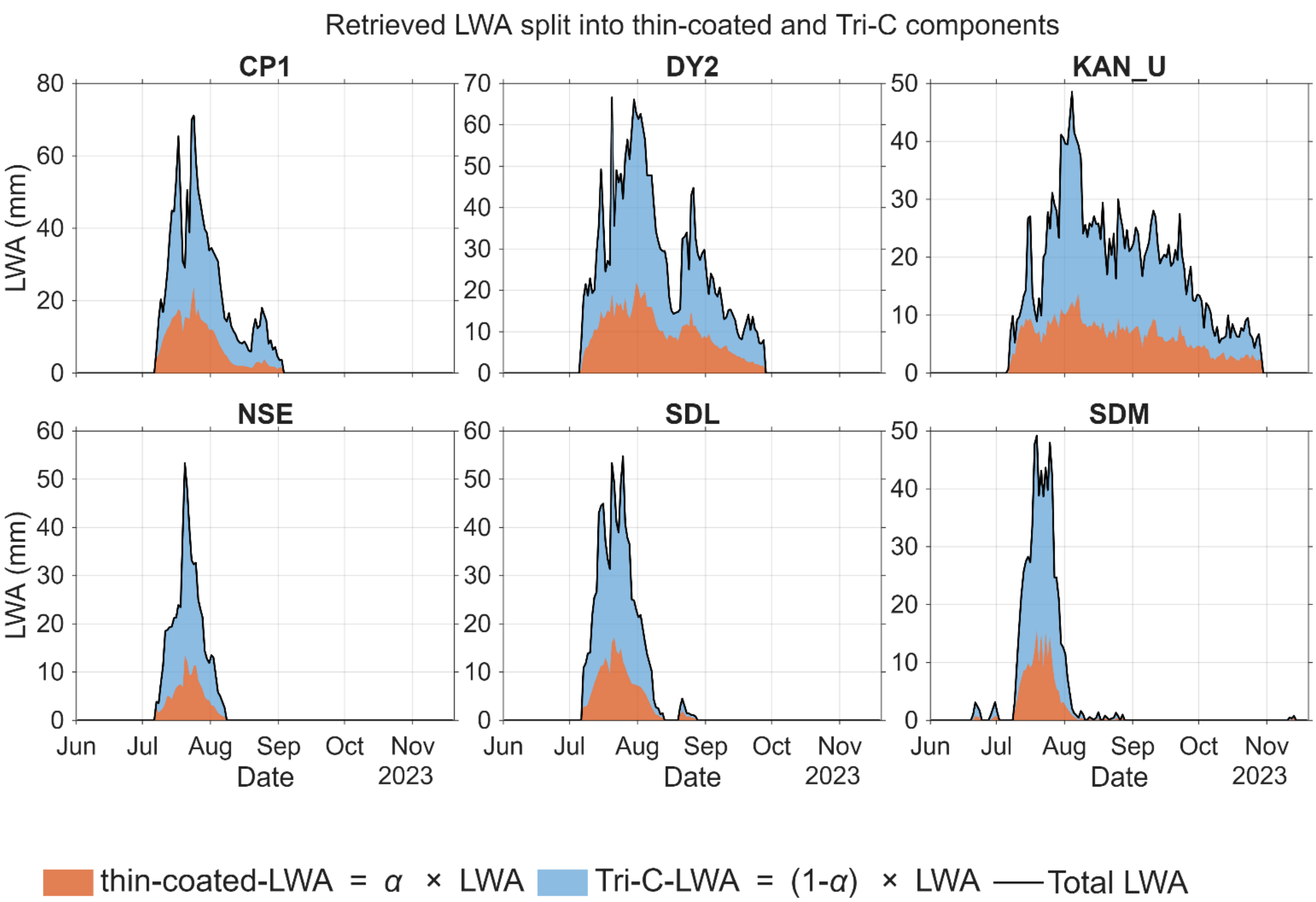

Figure 8: Decomposition of the retrieved LWA into thin-coated and Tri-C contributions at the six study sites during the 2023 melt season.

5 Discussion and Conclusions

5.1 Implications of Liquid Waer Morphology for L-Band LWA Retrievals

Most widely used wet snow mixing formulas do not explicitly represent the partitioning of liquid water between thin interfacial coatings and localized thicker water bodies. Our results show that this omission is not a minor detail. For the

https://doi.org/10.5194/egusphere-2026-3022
Preprint. Discussion started: 14 July 2026

representative case with LWC = 2%, and $\rho_s = 400 kg/m^3$, changing the thin-coated water fraction α from 0 to 1 increases the imaginary part of the effective permittivity by about a factor of 37. This strong sensitivity demonstrates that liquid water morphology exerts first-order control on L-band dielectric loss and, consequently, on the radiometric response of wet snow. Therefore, in the low-LWC regime relevant to Greenland percolation zone retrievals, the effective permittivity cannot be represented reliably as a function of LWC and snow density alone.

Stage	Newly Produced Meltwater Amount	Dominant Morphology	Key Process
Onset	Small	Thin-coated	New meltwater first appears as surface/interfacial water
Peak Melt	Large	Tri-C	Surface-bound storage is exceeded; additional meltwater shifts to thicker water bodies.
Late Season	Small	Mixed	New meltwater favors thin-coated water, but retained unfrozen Tri-C water reduces α

Table 2: Concise summary of the three seasonal stages of retrieved water morphology evolution.

The retrieval results further indicate that morphology is not merely a theoretical sensitivity parameter, but a seasonally evolving state variable. Although a single SMAP pass provides only two radiometric observables for three unknown wet state variables, the seasonally constrained inversion yields a physically coherent evolution across the six study sites. In particular, the retrieval suggests relatively larger thin-coated contributions at melt onset, Tri-C dominance during peak melt, and an incomplete late-season return toward thin-coated dominance because some liquid produced earlier in the season may remain unfrozen. This interpretation is consistent with the observed seasonal structure of the SMAP signal, the retrieved LWA evolution, and the meter scale wet layer thickness inferred for the six sites.

At the same time, the present framework should be viewed as an effective morphology aware retrieval rather than as a complete microphysical description of wet snow. The current retrieval adopts a fixed representative near surface density, uses a simplified two layer radiative transfer forward model, and interprets α as an effective morphology parameter rather than a directly observed geometric quantity. These simplifications make the present retrieval practical at regional scale, but they also define its current scope. A natural next step is to extend the forward model from two layers to a multilayer radiative transfer framework, in which each layer can have its own wetness, thickness, and morphology parameter α, so that vertical variations in liquid water morphology can be represented more realistically. Another important direction is to compare the inferred α with independent measurements or observations of wet snow microstructure and liquid water morphology when such data become available. Even with the present simplifications, the results here show that explicitly accounting for liquid

https://doi.org/10.5194/egusphere-2026-3022
Preprint. Discussion started: 14 July 2026

water morphology provides a more physically meaningful basis for L-band wet-snow retrieval than reliance on conventional mixing formulas alone.

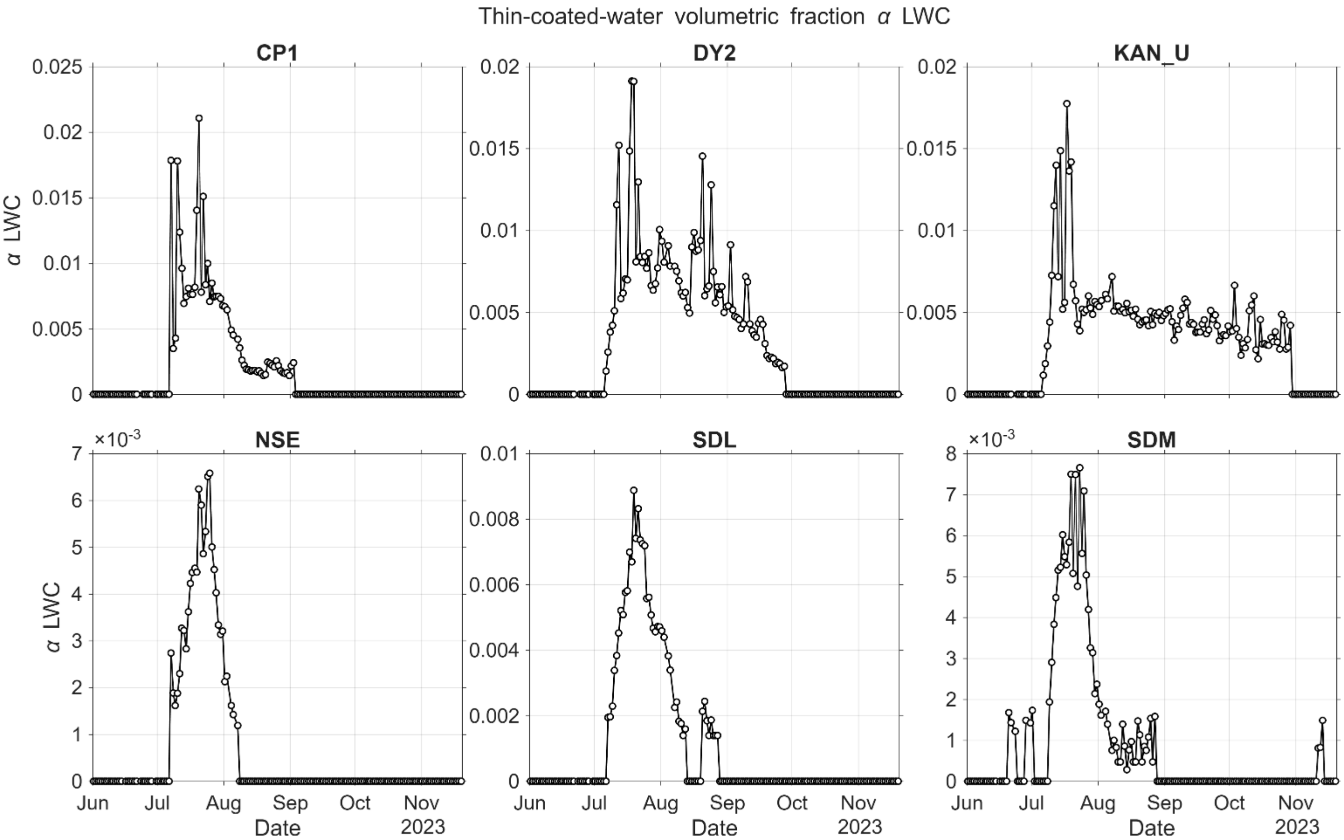

Figure 9: Retrieved thin-coated water volumetric fraction, $\alpha \cdot$ LWC, at the six study sites during the 2023 melt season.

5.2 Conclusions

In this study, we introduced a dual wet-snow model in which liquid water is partitioned between localized thicker Tri-C water and thin-coated interfacial water. The key contribution of the physical model is twofold: the computer-generated wet snow microstructure with explicit dual liquid water morphology provides a more realistic representation of low LWC wet snow microstructure, while the numerical solution of the 3D Maxwell equations provides a physically grounded route for calculating its effective permittivity.

The main conclusions are as follows. First, liquid water morphology has a very strong influence on the effective permittivity of low LWC wet snow. For a representative case with LWC = 2% and ρ_s = $400kg/m^3$, the imaginary part of the effective permittivity changes by about a factor of 37 as α varies from 0 to 1. Second, this morphology dependence can be incorporated into an efficient seasonally constrained retrieval framework by combining a numerical Maxwell permittivity database, a neural-network permittivity emulator, and a two-layer L-band radiative transfer model. Third, the resulting retrieval reproduces the main seasonal evolution of the observed SMAP morning pass brightness temperatures at the six

https://doi.org/10.5194/egusphere-2026-3022
Preprint. Discussion started: 14 July 2026

Greenland study sites and yields physically plausible LWA and wet layer thickness. Fourth, the inferred morphology evolution suggests relatively thin-coated water dominated conditions at melt onset, Tri-C dominance during peak melt, and an incomplete late-season return toward thin-coated dominance, likely because some earlier meltwater remains incompletely refrozen. Overall, these results indicate that future L-band retrievals of wet snow and firn should explicitly account for liquid-water morphology, rather than relying only on LWC and snow density.

Supplement link

The link to the supplement will be included by Copernicus, if applicable.

Author contributions

HJ: concept development, method design, code implementation, numerical simulations, data processing, formal analysis, figure preparation, original draft, paper revision; FB: electromagnetic modelling discussion, results discussion, paper revision; LT: supervision, concept development, method design, results discussion, paper revision; ZH: Bi-C/Tri-C microstructure and effective-permittivity modelling discussion, results discussion, paper revision; AH: processed data, results discussion, paper revision; AC: processed data, concept discussion, results discussion, paper revision.

Competing interests

The contact author has declared that none of the authors has any competing interests.

Acknowledgements

Part of this research was carried out at the Jet Propulsion Laboratory, California Institute of Technology under a contract with the National Aeronautics and Space Administration. © 2026. All rights reserved. We thank Dr. Nicole-Jeanne Schlegel of NOAA/OAR Geophysical Fluid Dynamics Laboratory (GFDL) for providing GEMB outputs which were adopted from (Hossan et al., 2025a). We also acknowledge the University of Michigan for providing access to the Ansys HFSS software license, which supported the full-wave electromagnetic simulations in this work.

Financial support

This research has been supported by the National Aeronautics and Space Administration (grant numbers 23-SMAP23-0032).

https://doi.org/10.5194/egusphere-2026-3022
Preprint. Discussion started: 14 July 2026

Review statement

The review statement will be added by Copernicus Publications listing the handling editor as well as all contributing referees according to their status anonymous or identified.

References

Ansys Hfss: Ansys Hfss Electronics Desktop Suite, https://doi.org/10.21227/PBEA-A051, n.d.

Brodzik, M. J., Long, D., and Hardman, M.: SMAP Radiometer Twice-Daily rSIR-Enhanced EASE-Grid 2.0 Brightness Temperatures, Version 2, https://doi.org/10.5067/YAMX52BXFL10, 2021.

Brun, E.: Investigation on Wet-Snow Metamorphism in Respect of Liquid-Water Content, Ann. Glaciol., 13, 22–26, https://doi.org/10.3189/S0260305500007576, 1989.

Chang, W., Tan, S., Lemmetyinen, J., Tsang, L., Xu, X., and Yueh, S. H.: Dense Media Radiative Transfer Applied to SnowScat and SnowSAR, IEEE J. Sel. Top. Appl. Earth Observations Remote Sensing, 7, 3811–3825, https://doi.org/10.1109/JSTARS.2014.2343519, 2014.

Charalampidis, C., Van As, D., Colgan, W. T., Fausto, R. S., Macferrin, M., and Machguth, H.: Thermal tracing of retained meltwater in the lower accumulation area of the Southwestern Greenland ice sheet, Ann. Glaciol., 57, 1–10, https://doi.org/10.1017/aog.2016.2, 2016.

Colbeck, S. C. and Parssinen, N.: Regelation and the Deformation of Wet Snow, J. Glaciol., 21, 639–650, https://doi.org/10.3189/S002214300003375X, 1978.

Colliander, A., Mousavi, M., Marshall, S., Samimi, S., Kimball, J. S., Miller, J. Z., Johnson, J., and Burgin, M.: Ice Sheet Surface and Subsurface Melt Water Discrimination Using Multi-Frequency Microwave Radiometry, Geophysical Research Letters, 49, e2021GL096599, https://doi.org/10.1029/2021GL096599, 2022.

Colliander, A., Mousavi, M., Kimball, J. S., Miller, J. Z., and Burgin, M.: Spatial and temporal differences in surface and subsurface meltwater distribution over Greenland ice sheet using multi-frequency passive microwave observations, Remote Sensing of Environment, 295, 113705, https://doi.org/10.1016/j.rse.2023.113705, 2023.

Denoth, A.: The Pendular-Funicular Liquid Transition and Snow Metamorphism, J. Glaciol., 28, 357–364, https://doi.org/10.3189/S0022143000011692, 1982.

Ding, Xiaolan Xu, and Leung Tsang: Electromagnetic Scattering by Bicontinuous Random Microstructures With Discrete Permittivities, IEEE Trans. Geosci. Remote Sensing, 48, 3139–3151, https://doi.org/10.1109/TGRS.2010.2043953, 2010.

Fausto, R. S., Van As, D., Mankoff, K. D., Vandecrux, B., Citterio, M., Ahlstrøm, A. P., Andersen, S. B., Colgan, W., Karlsson, N. B., Kjeldsen, K. K., Korsgaard, N. J., Larsen, S. H., Nielsen, S., Pedersen, A. Ø., Shields, C. L., Solgaard, A. M., and Box, J. E.: Programme for Monitoring of the Greenland Ice Sheet (PROMICE) automatic weather station data, Earth Syst. Sci. Data, 13, 3819–3845, https://doi.org/10.5194/essd-13-3819-2021, 2021.

https://doi.org/10.5194/egusphere-2026-3022
Preprint. Discussion started: 14 July 2026

Forster, R. R., Box, J. E., Van Den Broeke, M. R., Miège, C., Burgess, E. W., Van Angelen, J. H., Lenaerts, J. T. M., Koenig, L. S., Paden, J., Lewis, C., Gogineni, S. P., Leuschen, C., and McConnell, J. R.: Extensive liquid meltwater storage in firn within the Greenland ice sheet, Nature Geosci, 7, 95–98, https://doi.org/10.1038/ngeo2043, 2014.

Gardner, A. S., Schlegel, N.-J., and Larour, E.: Glacier Energy and Mass Balance (GEMB): a model of firn processes for cryosphere research, Geosci. Model Dev., 16, 2277–2302, https://doi.org/10.5194/gmd-16-2277-2023, 2023.

Greene, C. A., Gardner, A. S., Wood, M., and Cuzzone, J. K.: Ubiquitous acceleration in Greenland Ice Sheet calving from 1985 to 2022, Nature, 625, 523–528, https://doi.org/10.1038/s41586-023-06863-2, 2024.

Hallikainen, M., Ulaby, F., and Abdelrazik, M.: Dielectric properties of snow in the 3 to 37 GHz range, IEEE Trans. Antennas Propagat., 34, 1329–1340, https://doi.org/10.1109/TAP.1986.1143757, 1986.

Hornik, K., Stinchcombe, M., and White, H.: Multilayer feedforward networks are universal approximators, Neural Networks, 2, 359–366, https://doi.org/10.1016/0893-6080(89)90020-8, 1989.

Hossan, A., Colliander, A., Schlegel, N.-J., Harper, J., Andrews, L., Kolassa, J., Miller, J. Z., and Cullather, R.: Evaluation of wet snow dielectric mixing models for L-band radiometric measurement of liquid water content in Greenland's percolation zone, The Cryosphere, 19, 6077–6102, https://doi.org/10.5194/tc-19-6077-2025, 2025a.

Hossan, A., Colliander, A., Vandecrux, B., Schlegel, N.-J., Harper, J., Marshall, S., and Miller, J. Z.: Retrieval and validation of total seasonal liquid water amounts in the percolation zone of the Greenland ice sheet using L-band radiometry, The Cryosphere, 19, 4237–4258, https://doi.org/10.5194/tc-19-4237-2025, 2025b.

Houtz, D., Naderpour, R., Schwank, M., and Steffen, K.: Snow wetness and density retrieved from L-band satellite radiometer observations over a site in the West Greenland ablation zone, Remote Sensing of Environment, 235, 111361, https://doi.org/10.1016/j.rse.2019.111361, 2019.

Houtz, D., Mätzler, C., Naderpour, R., Schwank, M., and Steffen, K.: Quantifying Surface Melt and Liquid Water on the Greenland Ice Sheet using L-band Radiometry, Remote Sensing of Environment, 256, 112341, https://doi.org/10.1016/j.rse.2021.112341, 2021.

Huang, Z., Xu, H., Borah, F., Tsang, L., Medley, B., Johnson, J. T., and De Roo, R. D.: L-Band Full-Wave Simulations of the Effective Permittivity of Bi/Tri-Continuous Media With Applications to Firn Aquifer in Polar Regions and Terrestrial Wet Snow, IEEE Trans. Geosci. Remote Sensing, 62, 1–12, https://doi.org/10.1109/TGRS.2024.3455236, 2024.

Jin, J.-M.: The finite element method in electromagnetics, Third edition., John Wiley & Sons Inc, Hoboken. New Jersey, 846 pp., 2014.

Jones, S. B. and Friedman, S. P.: Particle shape effects on the effective permittivity of anisotropic or isotropic media consisting of aligned or randomly oriented ellipsoidal particles, Water Resources Research, 36, 2821–2833, https://doi.org/10.1029/2000WR900198, 2000.

Khan, S. A., Aschwanden, A., Bjørk, A. A., Wahr, J., Kjeldsen, K. K., and Kjær, K. H.: Greenland ice sheet mass balance: a review, Rep. Prog. Phys., 78, 046801, https://doi.org/10.1088/0034-4885/78/4/046801, 2015.

Khan, S. A., Bamber, J. L., Rignot, E., Helm, V., Aschwanden, A., Holland, D. M., Van Den Broeke, M., King, M., Noël, B., Truffer, M., Humbert, A., Colgan, W., Vijay, S., and Kuipers Munneke, P.: Greenland Mass Trends From Airborne and Satellite Altimetry During 2011–2020, JGR Earth Surface, 127, e2021JF006505, https://doi.org/10.1029/2021JF006505, 2022.

Mouginot, J., Rignot, E., Bjørk, A. A., Van Den Broeke, M., Millan, R., Morlighem, M., Noël, B., Scheuchl, B., and Wood, M.: Forty-six years of Greenland Ice Sheet mass balance from 1972 to 2018, Proc. Natl. Acad. Sci. U.S.A., 116, 9239–9244, https://doi.org/10.1073/pnas.1904242116, 2019.

Otosaka, I. N., Shepherd, A., Ivins, E. R., Schlegel, N.-J., Amory, C., Van Den Broeke, M. R., Horwath, M., Joughin, I., King, M. D., Krinner, G., Nowicki, S., Payne, A. J., Rignot, E., Scambos, T., Simon, K. M., Smith, B. E., Sørensen, L. S., Velicogna, I., Whitehouse, P. L., A, G., Agosta, C., Ahlstrøm, A. P., Blazquez, A., Colgan, W., Engdahl, M. E., Fettweis, X., Forsberg, R., Gallée, H., Gardner, A., Gilbert, L., Gourmelen, N., Groh, A., Gunter, B. C., Harig, C., Helm, V., Khan, S. A., Kittel, C., Konrad, H., Langen, P. L., Lecavalier, B. S., Liang, C.-C., Loomis, B. D., McMillan, M., Melini, D., Mernild, S. H., Mottram, R., Mouginot, J., Nilsson, J., Noël, B., Pattle, M. E., Peltier, W. R., Pie, N., Roca, M., Sasgen, I., Save, H. V., Seo, K.-W., Scheuchl, B., Schrama, E. J. O., Schröder, L., Simonsen, S. B., Slater, T., Spada, G., Sutterley, T. C., Vishwakarma, B. D., Van Wessem, J. M., Wiese, D., Van Der Wal, W., and Wouters, B.: Mass balance of the Greenland and Antarctic ice sheets from 1992 to 2020, Earth Syst. Sci. Data, 15, 1597–1616, https://doi.org/10.5194/essd-15-1597-2023, 2023.

Picard, G., Leduc-Leballeur, M., Banwell, A. F., Brucker, L., and Macelloni, G.: The sensitivity of satellite microwave observations to liquid water in the Antarctic snowpack, The Cryosphere, 16, 5061–5083, https://doi.org/10.5194/tc-16-5061-2022, 2022.

Rennermalm, Å. K., Hock, R., Covi, F., Xiao, J., Corti, G., Kingslake, J., Leidman, S. Z., Miège, C., Macferrin, M., Machguth, H., Osterberg, E., Kameda, T., and McConnell, J. R.: Shallow firn cores 1989–2019 in southwest Greenland's percolation zone reveal decreasing density and ice layer thickness after 2012, J. Glaciol., 68, 431–442, https://doi.org/10.1017/jog.2021.102, 2022.

Rumelhart, D. E., Hinton, G. E., and Williams, R. J.: Learning representations by back-propagating errors, Nature, 323, 533–536, https://doi.org/10.1038/323533a0, 1986.

Samimi, S., Marshall, S. J., and MacFerrin, M.: Meltwater Penetration Through Temperate Ice Layers in the Percolation Zone at DYE-2, Greenland Ice Sheet, Geophysical Research Letters, 47, e2020GL089211, https://doi.org/10.1029/2020GL089211, 2020.

Samimi, S., Marshall, S. J., Vandecrux, B., and MacFerrin, M.: Time-Domain Reflectometry Measurements and Modeling of Firn Meltwater Infiltration at DYE-2, Greenland, JGR Earth Surface, 126, e2021JF006295, https://doi.org/10.1029/2021JF006295, 2021.

Siddiqui, S. A., Hasler, M., Mössner, M., Van Putten, J., Schindelwig, K., and Nachbauer, W.: Detection of frictional meltwater on snow surface using a humidity indicator, CISS, 9, 010, https://doi.org/10.36950/2024.4ciss010, 2024.

https://doi.org/10.5194/egusphere-2026-3022
Preprint. Discussion started: 14 July 2026

Sihvola, A.: Electromagnetic Mixing Formulas and Applications, Institution of Engineering and Technology, https://doi.org/10.1049/PBEW047E, 1999.

The IMBIE Team: Mass balance of the Greenland Ice Sheet from 1992 to 2018, Nature, 579, 233–239, https://doi.org/10.1038/s41586-019-1855-2, 2020.

Tiuri, M., Sihvola, A., Nyfors, E., and Hallikaiken, M.: The complex dielectric constant of snow at microwave frequencies, IEEE J. Oceanic Eng., 9, 377–382, https://doi.org/10.1109/JOE.1984.1145645, 1984.

Ulaby, F. T. and Long, D. G.: Microwave radar and radiometric remote sensing, The University of Michigan Press, Ann Arbor, 984 pp., 2014.

Xu, X., Tsang, L., and Yueh, S.: Electromagnetic Models of Co/Cross Polarization of Bicontinuous/DMRT in Radar Remote Sensing of Terrestrial Snow at X- and Ku-band for CoReH2O and SCLP Applications, IEEE J. Sel. Top. Appl. Earth Observations Remote Sensing, 5, 1024–1032, https://doi.org/10.1109/JSTARS.2012.2190719, 2012.

Zhu, J., Tsang, L., and Xu, X.: Modeling of Scattering by Dense Random Media Consisting of Particle Clusters With DMRT Bicontinuous, IEEE Trans. Antennas Propagat., 71, 3611–3619, https://doi.org/10.1109/TAP.2023.3240562, 2023.